Catalysis Science & Technology

ROYAL SOCIETY OF CHEMISTRY

PAPER

View Article Online
View Journal | View Issue

Cite this: *Catal. Sci. Technol.*, 2025, **15**, 1122

Transition metal atoms embedded in monolayer $C_{13}N_3$ as OER/ORR bifunctional electrocatalysts†

Xiaoxue Yu,[a] Junkai Xu,[a] Yunhao Wang,[a] Jianjun Fang,*[a] Xianfang Yue,*[b] Breno R. L. Galvão *[c] and Jing Li *[a]

Received 29th September 2024,
Accepted 5th January 2025

DOI: 10.1039/d4cy01160k

rsc.li/catalysis

Developing bifunctional electrocatalysts for efficiently catalyzing the oxygen evolution/reduction reaction (OER/ORR) is essential for water electrolysis and other processes. Herein, we have investigated the OER and ORR performance of monolayered TM-$C_{13}N_3$ by first-principles calculations, where TM includes Cr, Mn, Fe, Co, Ni, Cu, Ru, Rh, Pd, Ag, Os, Ir, Pt, and Au. The results show that Pt-$C_{13}N_3$ has excellent bifunctional OER/ORR activity with overpotentials of 0.27 V for the OER and 0.39 V for the ORR. In addition, volcano plots and contour maps based on the linear relationship between the adsorption energies of oxygenated intermediates were established to characterize the OER/ORR activity trends of TM-$C_{13}N_3$. The origin of the OER/ORR activity is revealed by analyzing Bader charges, the d-band center, and the crystal orbital Hamiltonian population (COHP).

I. Introduction

The overconsumption of fossil fuels has greatly impacted human production and life, and it is vital to develop green energy sources to replace them.[1,2] Hydrogen energy, as the most ideal alternative to fossil fuels, has several advantages: it is non-polluting, recyclable and has a high calorific value.[3–6] The hydrogen energy cycle can be realized by the following technologies: water electrolysis reaction,[7] fuel cells,[8] and rechargeable metal–air batteries,[9] among others. However, the kinetics of the oxygen evolution reaction (OER) and the oxygen reduction reaction (ORR), the two core reactions of these technologies, are sluggish.[10] In industry, Pt and RuO_2 are still the most popular OER and ORR electrocatalysts.[11,12] However, these noble metal catalysts have certain drawbacks, such as high cost, instability, and low earth abundance compared to Fe, Co, and Ni, which limit their commercial application.[13] Furthermore, these noble metal catalysts are also unifunctional catalysts.[14] For example, although Pt(111) can catalyze the ORR effectively, it is less effective in catalyzing the OER. For this reason, here we try to find a single catalyst to replace both noble-metal ones. The design of efficient OER and ORR bifunctional catalysts is crucial to realize large-scale electrolytic water recycling applications and solve the clean energy shortage.[15–19]

The proposal of single-atom catalysts (SACs) opens an avenue to design novel catalysts.[20] On the one hand, the active sites of SACs reduce to the atomic scale to maximize the use of metal atoms.[21] Compared to bulk catalysts, nanocatalysts and subnanocatalysts, the utilization rate of metal atoms increases to 100%. On the other hand, the activity of the SACs is modulated by adjusting the coordination environment of the carrier material.[22,23]

Designing single-atom catalysts around C_xN_y materials is gradually becoming a popular research topic. For example, Zhang *et al.* reported anchoring a series of transition metal atoms on a C_2N monolayer.[12] Almost all TM_x@C_2N catalysts exhibit metallicity and have excellent charge transfer capabilities. Notably, Mn_1@C_2N was found to act as a bifunctional electrocatalyst for both the hydrogen evolution reaction (HER) and OER.[12] The feasibility of a single transition metal embedded in defective g-C_3N_4 for bifunctional electrocatalysis was reported by Niu *et al.*[24] The rhodium doped defective g-C_3N_4 with N vacancy (Rh/V_N-CN) was found to exhibit low overpotentials of 0.32 V and 0.43 V for the OER and ORR, respectively, and was considered as an excellent bifunctional catalyst. Zhou *et al.*[25] reported that transition metal atoms loaded on C_9N_4 monolayers can bond with surrounding nitrogen atoms to stabilize the structure. The diffusion barrier of doped TM from its stable adsorption site to neighboring sites is high. In their work, Ni@C_9N_4 was found to be a promising bifunctional electrocatalyst, with the lowest overpotential for the OER of 0.31 V.

[a] *School of Physics and Physical Engineering, Qufu Normal University, Qufu, Shandong 273165, China. E-mail: jian-junfang@163.com, jli@qfnu.edu.cn*
[b] *Department of Physics and Information Engineering, Jining University, Qufu 273155, China. E-mail: xfyuejnu@jnxy.edu.cn*
[c] *Centro Federal de Educação Tecnológica de Minas Gerais, CEFET-MG, Av. Amazonas 5253, 30421-169 Belo Horizonte, Minas Gerais, Brazil. E-mail: brenogalvao@gmail.com*

† Electronic supplementary information (ESI) available. See DOI: https://doi.org/10.1039/d4cy01160k

Recently, Tan *et al.*[26] reported a novel monolayered $C_{13}N_3$ material, and found that the Gibbs free energies of $C_{13}N_3$ are all lower than those of all synthesized 2D carbon nitride materials (g-CN, C_2N, C_3N, g-C_3N_4), and showed that it has great potential for future high-performance electronics applications. $C_{13}N_3$ is a conductor and, for this reason, also has potential as an electrocatalyst. Moreover, it is a porous carbon nitride material with a high specific surface area, providing increased catalytic active sites. It presents a marked enhancement in catalytic activity when employed as a visible-light photocatalyst for hydrogen evolution.[27]

In this work, we investigated the potential of SACs with stoichiometry TM-$C_{13}N_3$ (TM═Cr, Mn, Fe, Co, Ni, Cu, Ru, Rh, Pd, Ag, Os, Ir, Pt or Au) for the OER and ORR by first-principles calculations. First, we evaluated the stability as well as the OER and ORR activities of the proposed catalysts. Next, the trend in their catalytic activity was illustrated by volcano plots and contour maps. They predicted not only the optimal activity, but also the potential-determining step (PDS) for the OER and ORR. Among the results, we highlight that Pt-$C_{13}N_3$ could be used as a bifunctional OER/ORR catalyst with OER and ORR overpotentials of 0.27 and 0.39 V, respectively. Finally, the origin of the excellent OER and ORR catalytic activity of Pt-$C_{13}N_3$ was rationalized by analysing the d-band center and crystal orbital Hamiltonian population (COHP) of the proposed materials.

II. Methods

A. Calculation details

In this work, all calculations were performed in the Vienna *ab initio* simulation package (VASP) using the DFT method.[28,29] The ion–electron interaction was described by the projector augmented wave (PAW) method with a cutoff energy of 500 eV.[30] The exchange–correlation interaction is determined by the Perdew–Burke–Ernzerhof (PBE)[31] functional in the generalized gradient approximation (GGA), and the GGA + U method is employed to consider the correction of electron correlation,[32] with an empirical value of U = 3 for the TM-$C_{13}N_3$. The thickness of the vacuum layer between the two TM-$C_{13}N_3$ sheets was set to 20 Å to avoid interlayer interactions. The convergence thresholds for energy and force are set to 10^{-5} eV and 0.02 eV Å^{-1}, respectively, thus ensuring that all atomic positions are fully relaxed. A 4 × 4 × 1 gamma-centered k-point grid is used. In addition, the crystal orbital Hamiltonian population (COHP) of the bond strength of the catalyst to the reaction intermediates was calculated using the Lobster software.[33] *Ab initio* molecular dynamics (AIMD) simulations were used to evaluate the thermal stability of TM-$C_{13}N_3$ at a temperature of 1000 K using a step of 1 fs for 5 ps.[34,35] Charge transfer is analyzed by Bader charge analysis.[36]

B. Free energy diagram for the OER and ORR

The OER catalytic properties of TM-$C_{13}N_3$ were investigated considering the four-electron pathway under acidic conditions (pH = 0)[37,38] and employing the computational hydrogen electrode (CHE) model.[39] In the first step, TM-$C_{13}N_3$ (denoted as *) takes an H_2O molecule and decomposes it to form an $H^+ + e^-$ pair and *OH. In the second step, the *OH intermediate dissociates into *O, releasing a second $H^+ + e^-$ pair. In the third step, *O reacts with another water molecule to form *OOH and releases another $H^+ + e^-$ pair. In the last step, finally, *OOH dissociates into O_2 releasing the fourth $H^+ + e^-$ pair. The four elementary steps of the OER can be described as:

$$* + H_2O(l) \rightarrow *OH + H^+ + e^- \quad (1)$$

$$*OH \rightarrow *O + H^+ + e^- \quad (2)$$

$$*O + H_2O(l) \rightarrow *OOH + H^+ + e^- \quad (3)$$

$$*OOH \rightarrow * + O_2(g) + H^+ + e^- \quad (4)$$

To calculate the free energy changes of the above reactions, the free energy (G) of the $H^+ + e^-$ pair can be replaced by half of that of an H_2 molecule at 298 K, following the CHE model.[39] The free energy of gas-phase O_2 is written in terms of the free energies of H_2O and H_2 molecules (G_{H_2O} and G_{H_2}) using the experimental value for the energy of the $2H_2O \rightarrow O_2 + 2H_2$ reaction (4.92 eV). Therefore, the free energy change at each step can be written as:

$$\Delta G_1 = \Delta G_{*OH} \quad (5)$$

$$\Delta G_2 = \Delta G_{*O} - \Delta G_{*OH} \quad (6)$$

$$\Delta G_3 = \Delta G_{*OOH} - \Delta G_{*O} \quad (7)$$

$$\Delta G_4 = 4.92 - \Delta G_{*OOH} \quad (8)$$

where ΔG_{*OH}, ΔG_{*O}, and ΔG_{*OOH} denote the adsorption energies of *OH, *O, and *OOH. These adsorption energies are defined as:

$$\Delta G_{*OH} = G_{*OH} - G_* - G_{H_2O} + 1/2G_{H_2} \quad (9)$$

$$\Delta G_{*O} = G_{*O} - G_* - G_{H_2O} + G_{H_2} \quad (10)$$

$$\Delta G_{*OOH} = G_{*OOH} - G_* - 2G_{H_2O} + 3/2G_{H_2} \quad (11)$$

where G_*, G_{*OH}, G_{*O}, and G_{*OOH} denote the free energies of *, *OH, *O, and *OOH, respectively. Each of these Gibbs free energies (G) can be calculated as:

$$G = E_{DFT} + ZPE + \Delta U - T\Delta S + G_U + G_{pH} \quad (12)$$

where E_{DFT} corresponds to the energy calculated by DFT and ZPE is the zero-point energy. ΔU denotes the internal energy

increment from 0 K to 298.15 K. ΔS is the entropy change, and $G_U = -n_e U$, where n_e denotes the number of electrons and U is the electrode potential. $G_{pH} = k_B T \times \ln 10 \times pH$ is the proton concentration free energy correction formula, where k_B is the Boltzmann constant and T is the absolute temperature of 298.15 K (room temperature), and the pH value is set to 0 in an acidic medium.

The step with the highest increase in energy for the OER process is defined as the potential-determining step (PDS). To evaluate the catalytic activity, the OER overpotential (η_{OER}) is defined as:

$$\eta_{OER} = \frac{\max(\Delta G_1, \Delta G_2, \Delta G_3, \Delta G_4)}{e} - 1.23 \quad (13)$$

where 1.23 V is the equilibrium potential.

The ORR process is the reverse OER. Therefore, the overpotential of the ORR (η_{ORR}) can be written as:

$$\eta_{ORR} = -\frac{\min(\Delta G_1, \Delta G_2, \Delta G_3, \Delta G_4)}{e} + 1.23 \quad (14)$$

C. Construction of Pourbaix diagrams

Pourbaix diagrams reveal a clear relationship between chemically stable structures in electrochemical systems as pH and electrode potential (U).[40,41] In this study, we constructed Pourbaix diagrams for Pt-$C_{13}N_3$ by calculating the free energy changes of adsorbed species (*i.e.*, *O, *OH, and *OOH). Here, * refers to the corresponding surface catalytic site. For all adsorbed species, each reaction can be written as:

$$* + H_2O \rightarrow *O + 2(H^+ + e^-) \quad (15)$$

$$* + H_2OH \rightarrow *O + H^+ + e^- \quad (16)$$

$$* + 2H_2O \rightarrow *OOH + 3(H^+ + e^-) \quad (17)$$

Then, adsorption energies (ΔE) for each species were calculated at zero potential and standard conditions to obtain the following equations:

$$\Delta E_{*O} = E_{*O} + E_{H_2} - E_* - E_{H_2O} \quad (18)$$

$$\Delta E_{*OH} = E_{*OH} + 0.5E_{H_2} - E_* - E_{H_2O} \quad (19)$$

$$\Delta E_{*OOH} = E_{*OOH} + 1.5E_{H_2} - E_* - 2E_{H_2O} \quad (20)$$

According to the free energy equation, the ΔG of a substance as a function of pH and U can be defined as follows:

$$\Delta G(pH, U) = \Delta E + \Delta ZPE - T\Delta S - \nu(H^+)\cdot k_B T\cdot \ln 10\cdot pH - \nu(e^-)\cdot eU \quad (21)$$

where k_B is the Boltzmann constant, and the value of $k_B T\cdot \ln 10$ is 0.059; $\nu(H^+)$ and $\nu(e^-)$ are the values for the stoichiometric coefficients of the transferred protons and electrons of the corresponding adsorption processes (eqn (15)–(17)), respectively.

III. Results and discussion

A. Structure and stability of TM-$C_{13}N_3$

We built a carbon nitride monolayer of $C_{13}N_3$ as shown in Fig. 1(a) and (b). Crystal structures can be constructed from graphene superlattices by removing the six-membered rings of C atoms and replacing the edge C atoms with N atoms. The lattice parameter of $C_{13}N_3$ is $a = b = 10.72$ Å. In order to perform the calculations on the expected TM-$C_{13}N_3$ catalysts, different metals were allowed to be embedded in the edges of the aperture to bond with two N atoms as shown in Fig. 1(c). The selected metals were Cr, Mn, Fe, Co, Ni, Cu, Ru, Rh, Pd, Ag, Os, Ir, Pt, and Au.

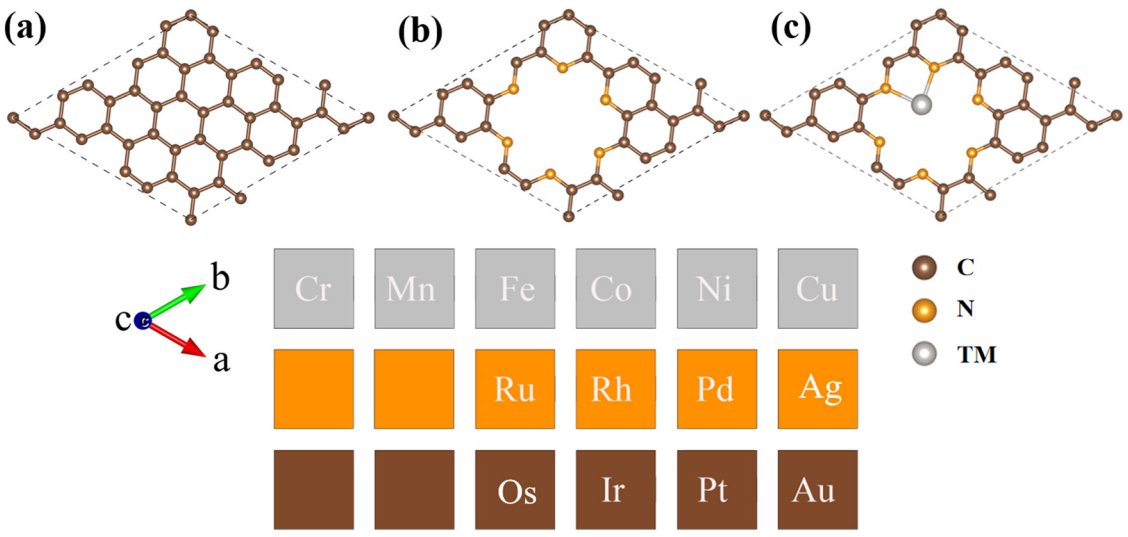

Fig. 1 Schematic structures of (a) graphene, (b) $C_{13}N_3$ and (c) TM-$C_{13}N_3$, and embedded TM atoms.

After full geometrical optimization, we calculate the binding energy (E_{bind}) and dissolution potential (U_{diss}, *versus* SHE) to evaluate the stability of TM-$C_{13}N_3$. Similar to previous work,[42–45] the binding energy (E_{bind}) is expressed as:

$$E_{bind} = E_{tot} - E_{C_{13}N_3} - E_{TM\text{-}single} \quad (22)$$

where E_{tot} is the total energy of TM-$C_{13}N_3$, $E_{C_{13}N_3}$ denotes the energy of $C_{13}N_3$ (without the metal atom), and $E_{M\text{-}single}$ refers to the energy of an isolated transition metal atom (gas-phase). A negative E_{bind} indicates the thermodynamic stability of the catalysts, with a more negative E_{bind} indicating a stronger binding of the metal atoms to the substrate. The specific values of E_{bind} are shown in ESI† Table S1 and Fig. 2. Except for the coinage metals and Pd, the magnitude of all binding energies is higher than 4 eV. Even for the weakest binding energy (gold), we observe a sufficiently high metal–$C_{13}N_3$ interaction.

Furthermore, we calculated the cluster energy ($E_{cluster}$) to describe the aggregation possibility of these anchored transition metal atoms on the TM-$C_{13}N_3$ SACs, which is defined as:

$$E_{cluster} = E_{bind} - E_{coh} \quad (23)$$

where E_{coh} is the cohesive energy of the TM atoms ($E_{coh} = E_{M\text{-}bulk}/n - E_{M\text{-}single}$), and $E_{M\text{-}bulk}$ refers to the energy of the transition metal bulk and n is the number of TM atoms in a unit bulk. If $E_{cluster}$ is less than 0, metal atoms do not readily aggregate to form clusters during preparation and cyclic catalysis, and *vice versa*. As shown in Fig. S1 (ESI†), Cr-$C_{13}N_3$, Mn-$C_{13}N_3$, Cu-$C_{13}N_3$, Pt-$C_{13}N_3$, and Ag-$C_{13}N_3$ conform to $E_{cluster} > 0$, indicating that they do not readily aggregate to form clusters during preparation and cyclic catalysis.

Next, we evaluate the electrochemical stability of the catalyst by using the dissolution potential U_{diss} ($U_{diss} = U_{diss\text{-}bulk} - E_{cluster}/n_e$). $U_{diss\text{-}bulk}$ and n_e represent the standard dissolution potentials of TM bulk and the number of transferred electrons during the process of dissolution, respectively. The catalyst needs to satisfy two conditions simultaneously: E_{bind} less than 0 and U_{diss} greater than 0. As shown in Fig. 2, all the binding energies are negative and the dissolution potentials are positive, demonstrating the stability of TM-$C_{13}N_3$ systems.

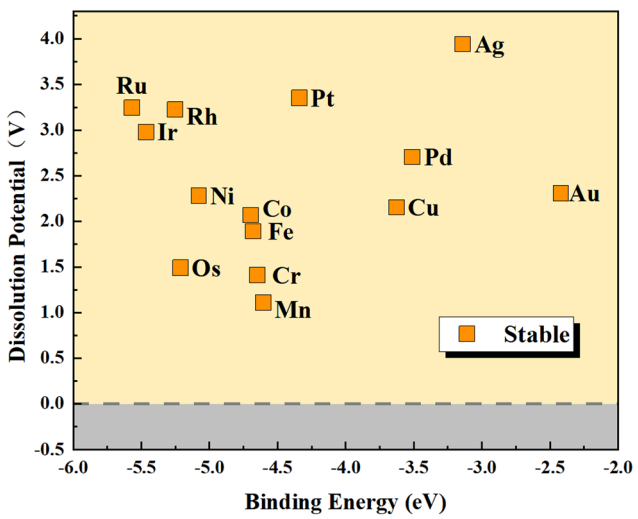

Fig. 2 E_{bind} and U_{diss} calculated by the TM-$C_{13}N_3$ system.

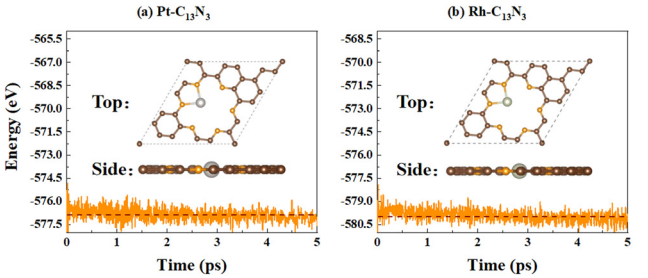

Fig. 3 Variation of energy as a function of time in the AIMD simulation within 5 ps at 1000 K for (a) Pt-$C_{13}N_3$ and (b) Rh-$C_{13}N_3$.

In addition, AIMD simulations at 1000 K lasting 5 ps were performed with Pt-$C_{13}N_3$ and Rh-$C_{13}N_3$ as examples. Fig. 3 shows that the energies of Pt-$C_{13}N_3$ and Rh-$C_{13}N_3$ oscillate within a 3 eV interval, which is not sufficient to overcome the binding energy, further illustrating the thermal stability of the TM-$C_{13}N_3$ materials.

On the basis of AIMD simulations, we calculated the bond lengths between the metal Pt and the connected N atoms, as shown in Fig. 4. During the sustained 5 ps, the bond length oscillates around 2 Å and it seems that the peaks in the two graphs (N_1-TM and N_2-TM) do not occur at the same time. This means that one of these two variables is always small, and thus it only goes to neighboring sites.

Moreover, in order to further understand the stability of Pt-based catalysts, we used climbing image nudged elastic band (CI-NEB)[46] to evaluate the barrier for diffusion of the Pt atom from the cavity of g-$C_{13}N_3$ to the bridge of carbon atoms, as shown in Fig. 5. The results reveal that the diffusion not only is highly endergonic with an energy demand of 2.69 eV, but also requires a very large diffusion barrier of 2.95 eV. The significantly large binding energies and negligible structural deformation around 1000 K, and large diffusion barrier indicate the enhanced thermal stability of Pt-$C_{13}N_3$ catalysts.

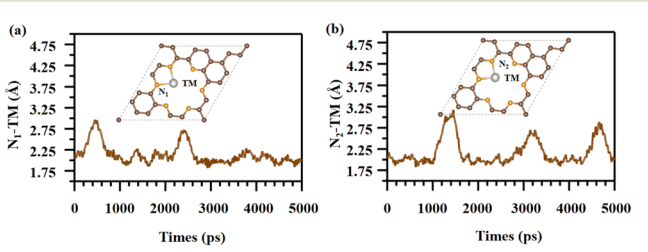

Fig. 4 Dynamic evolution of (a) N_1-Pt and (b) N_2-Pt bond length in the AIMD simulations.

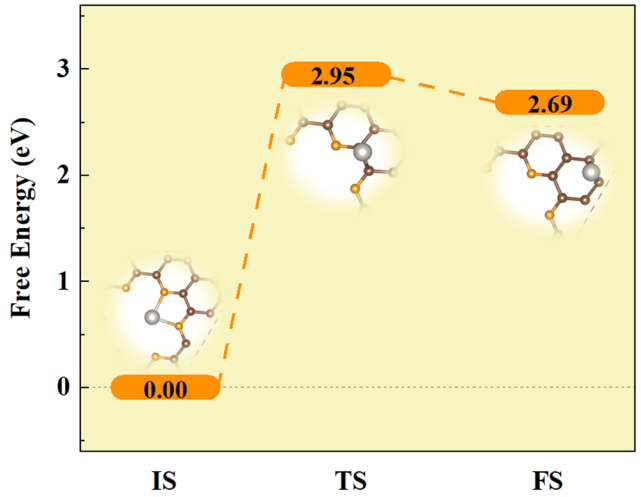

Fig. 5 The energy pathway of the anchored Pt atom to diffuse to the neighboring site in $C_{13}N_3$ and the optimized structures of the initial state (IS), transition state (TS) and final state (FS).

B. OER/ORR performance

After determining the stability of TM-$C_{13}N_3$, we further evaluated the catalytic performance of TM-$C_{13}N_3$. For that, we first calculate the adsorption energy of each oxygen-containing intermediate (*O, *OH, and *OOH), which is shown in ESI† Table S2. According to previous studies,[47] similar TM-O bonds between the metal and oxygenated intermediates resulted in a similar adsorption behavior for all three species. For this reason, the adsorption energies of OH, O, and OOH may be correlated *via* linear relationships. As shown in Fig. 6, this has also been observed within our results for the TM-$C_{13}N_3$ substrates. The relationship between ΔG_{*O} *vs.* ΔG_{*OH} can be expressed as $\Delta G_{*O} = 1.44 + 1.30$ with a high coefficient of determination ($R^2 = 0.72$). The relationship between ΔG_{*OOH} *vs.* ΔG_{*OH} can be expressed as $\Delta G_{*OOH} = 0.88\Delta G_{*OH} + 3.24$ ($R^2 = 0.91$).

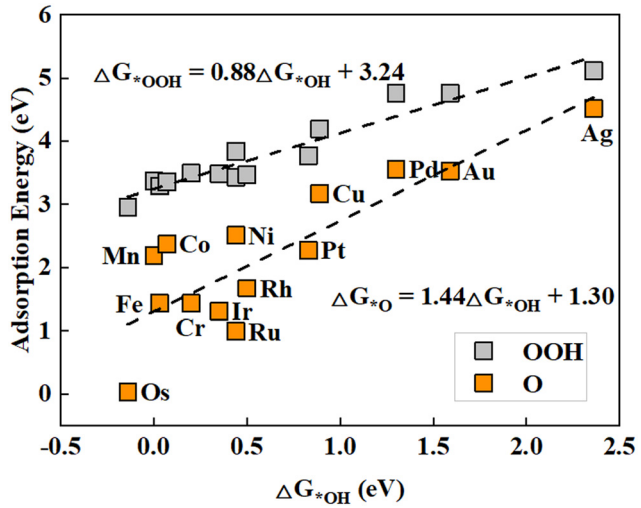

Fig. 6 Scaling relations between the adsorption energies of intermediates (ΔG_{*O} *vs.* ΔG_{*OH} in orange; ΔG_{*OOH} *vs.* ΔG_{*OH} in gray) on TM-$C_{13}N_3$.

The free energy changes for each step of the ORR and OER on TM-$C_{13}N_3$ were calculated as eqn (5)–(8) and are shown in ESI† Table S3 and Fig. 7(a) and (b), in which the equilibrium potential of 1.23 V was applied in Fig. 7(a) and (b). While the OER proceeds following * + H_2O → *OH → *O → *OOH → * + O_2, the ORR process occurs in the reverse direction (* + O_2 → *OOH → *O → *OH → * + H_2O). We recall that the rate of the OER or the ORR is limited by the PDS, which has the largest free energy change. This crucial step is not the same for the different metals, as can be seen by analyzing the energy changes in Fig. 7. Taking Cr-$C_{13}N_3$ as an example, the OER process is mainly hindered by the *O → *OOH step, while the ORR one is hindered by *OH → * + H_2O.

The ORR and OER overpotentials of the candidates are summarized in Fig. 7(c). Among all the TM-$C_{13}N_3$ samples, Pt-$C_{13}N_3$ had both the lowest OER overpotential ($\eta_{OER} = 0.27$ V) and the lowest ORR overpotential ($\eta_{ORR} = 0.39$ V). Furthermore, the overpotentials for the OER and ORR on Pt-$C_{13}N_3$ are even lower than those of conventional noble metal catalysts such as Pt ($\eta_{ORR} = 0.45$ V) and RuO_2 ($\eta_{OER} = 0.42$ V).[11,48] Note that even though our proposed catalyst also includes the noble metal Pt in its structure (as the conventional catalyst for the ORR), its percentage in both mole and weight is substantially lower, turning the material proposed here potentially cheaper due to the inclusion of earth-abundant elements. Even more promising is its usage as a bifunctional catalyst that can work for both the OER and ORR in the same apparatus. In addition to Pt-$C_{13}N_3$, Cu-$C_{13}N_3$ also showed considerable ORR performance with an overpotential of 0.5 V, suggesting that it may also be an excellent ORR catalyst, without including expensive metals.

Although the four-electron associative pathway was discussed above, we also evaluated the possibility of the two-electron mechanism occurring in Pt-$C_{13}N_3$, by calculating the energy barrier of O_2 dissociation. We considered the reaction pathways for O_2 dissociation on Pt-$C_{13}N_3$ as shown in ESI† Fig. S2. The energy barrier for O_2 dissociation on Pt-$C_{13}N_3$ is 2.93 eV, which is much higher than the 0.53 eV on Pt(111).[49] Our results indicate that the dissociative ORR is unlikely to happen on Pt-$C_{13}N_3$.

C. Trend of catalytic activity

According to Sabatier's principle,[50] too strong or too weak adsorption of intermediates on TM-$C_{13}N_3$ may negatively affect its catalytic performance. If the intermediates are too strongly adsorbed on the catalyst, the reaction products will be difficult to desorb. In contrast, if the adsorption is too weak, it will hinder the activation of the intermediates. Thus, a volcano plot may represent the catalytic activity, and the best catalysis can be located at the top. Based on the above linear relationship, the descriptors of the OER and ORR volcano plots are $\Delta G_{*O} - \Delta G_{*OH}$ and ΔG_{*OH}, respectively, as

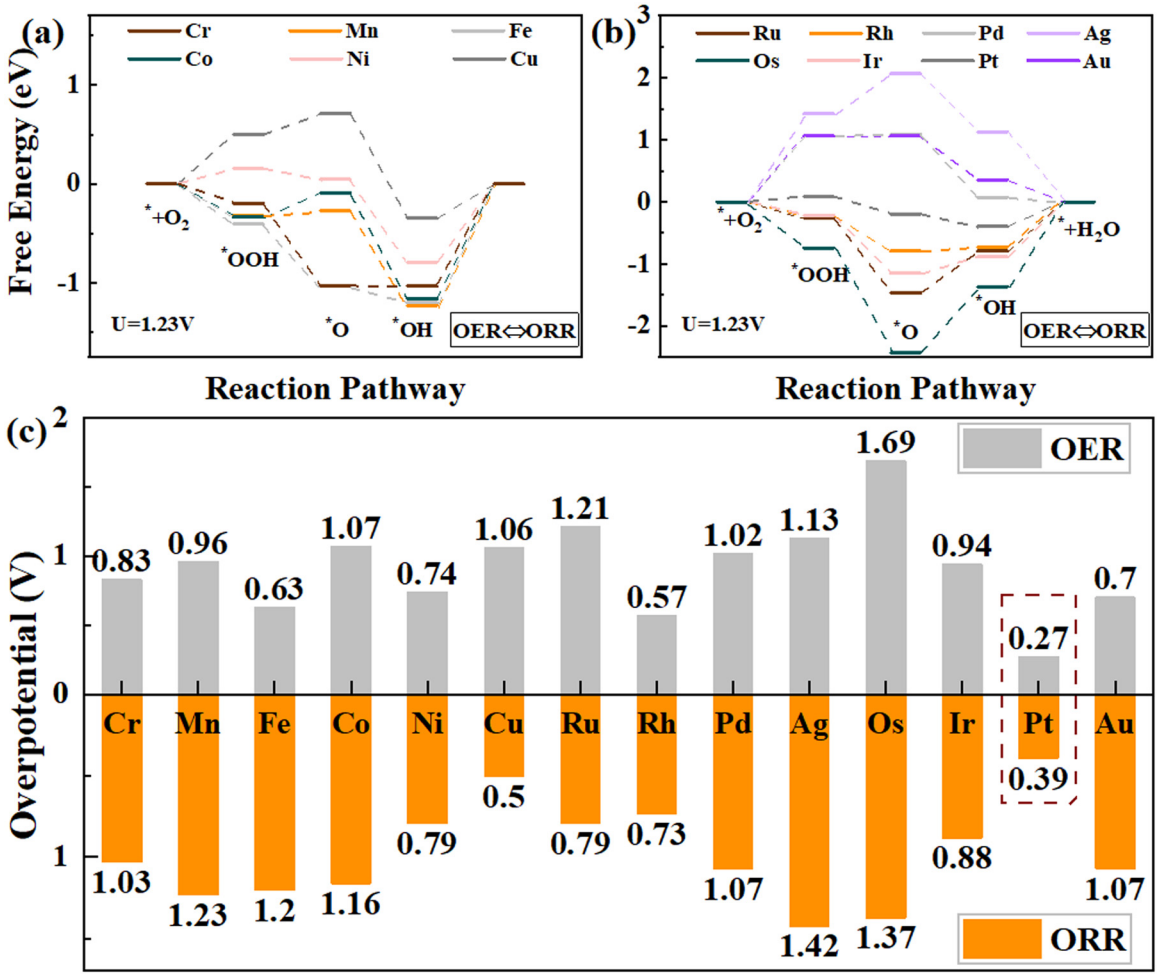

Fig. 7 OER and ORR free energy diagrams of $TM_{13}N_3$, (a) from Cr to Cu and (b) from Ru to Au. The OER is from left to right, while the ORR is contrary. The equilibrium potential of 1.23 V is applied. (c) The OER and ORR overpotentials of $TM_{13}N_3$ (from Cr to Au).

shown in Fig. 8(a) and (b). The best OER catalyst possesses a $\Delta G_{*O} - \Delta G_{*OH}$ value of 1.44 eV, while the ΔG_{*OH} value of 0.83 eV is required for the best ORR catalyst. It can be seen that Pt-$C_{13}N_3$ has the most potential as a bifunctional catalyst among all the candidates. The corresponding structures of the oxygenated intermediates (*OH, *O, and *OOH) adsorbed on Pt-$C_{13}N_3$ are shown in Fig. 8(c). The PDSs of the OER and ORR for different SACs are also shown in Fig. 8(a) and (b). Clearly, the two main PDSs for the OER are step 2 (*OH → *O) and step 3 (*O → *OOH). The two main ORR PDSs are step 1 (* + O_2 → *OOH) and step 4 (*OH → * + H_2O).

In this case, the linear relationships of the OER and ORR with ΔG_{*OH} and $\Delta G_{*O} - \Delta G_{*OH}$ were established to describe the catalyst activity. As shown in Fig. 9(a) and (b), contour maps of OER and ORR activities on TM-$C_{13}N_3$ can be established when ΔG_{*OH} and $\Delta G_{*O} - \Delta G_{*OH}$ are selected as descriptors. In previous studies, contour plots have been widely used to characterize catalyst activity trends.[51,52] Obviously, Pt-$C_{13}N_3$ as the best bifunctional catalyst is located at the best position of the contour plot with η_{OER} of 0.27 and η_{ORR} of 0.39. Overall, Pt-$C_{13}N_3$ exhibited low overpotentials for the OER and ORR, elucidating its excellent catalytic performance for the OER and ORR.

D. Origin of catalytic activity

We now rationalize the origin of the OER and ORR activities of TM-$C_{13}N_3$ by studying the electronic structure of the proposed materials. The charge transfer of the N atoms of $C_{13}N_3$, Pt-$C_{13}N_3$, and Os-$C_{13}N_3$ is given in the Bader charge analysis as shown in Fig. 10. We have chosen these metals because Pt-$C_{13}N_3$ possesses the best bifunctional catalytic activity, while Os-$C_{13}N_3$ exhibits the least desirable performance. First, we note that for both of the TM-$C_{13}N_3$ samples, the two nitrogen atoms bonded to the metal show an increase in charge compared to $C_{13}N_3$, while the other nitrogen atoms show a reduction. It can be seen that Pt induces a stronger charge transfer than Os. This suggests that charge transfer is an important descriptor for evaluating catalytic activity.

Fig. 11 shows the partial density of states (PDOS) of the d orbitals of the transition metal atoms in TM-$C_{13}N_3$ with the position of the d-band center marked. The specific values for

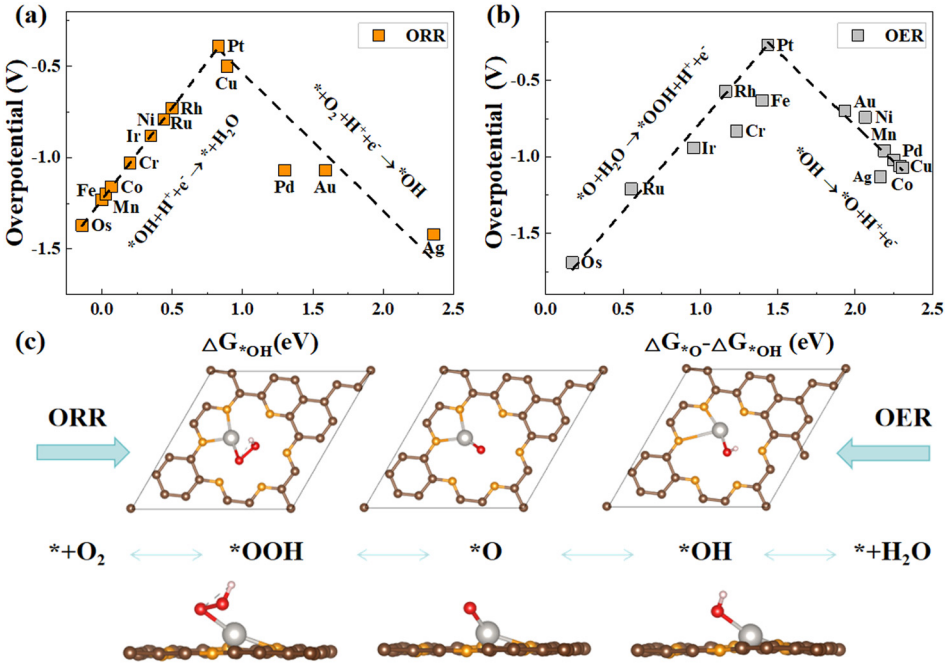

Fig. 8 (a) Volcano plot for the OER on TM-$C_{13}N_3$ with $-\eta_{OER}$ *vs.* ΔG_{*OH}. (b) Volcano plot for the ORR on TM-$C_{13}N_3$ with $-\eta_{ORR}$ *vs.* $\Delta G_{*O} - \Delta G_{*OH}$. The potential-determining steps of the OER and ORR are labeled. (c) Structures of intermediates (*OH, *O, and *OOH) of the OER and ORR adsorbed on Pt-$C_{13}N_3$.

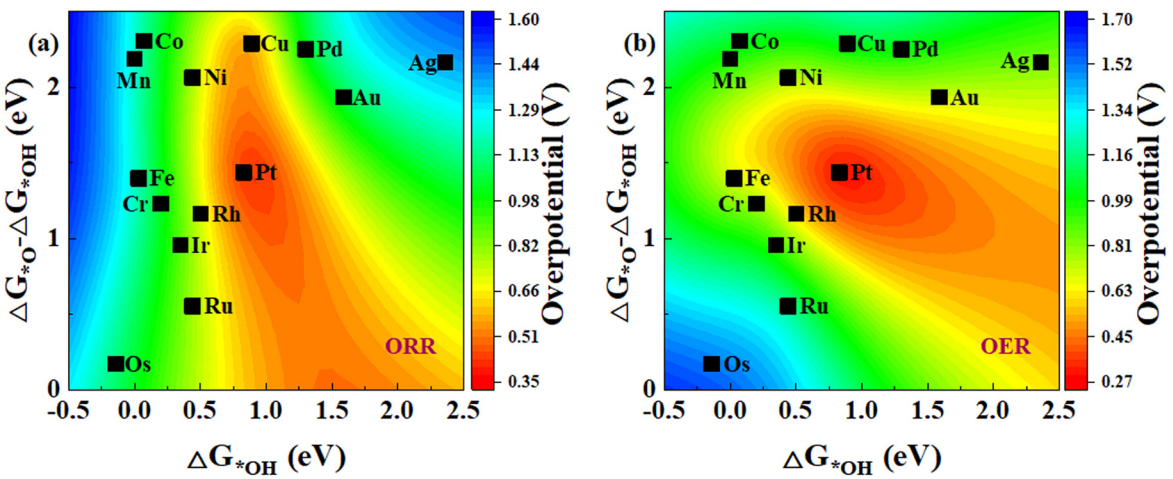

Fig. 9 The contour maps of (a) OER and (b) ORR activity trends on TM-$C_{13}N_3$, with ΔG_{*OH} and $\Delta G_{*O} - \Delta G_{*OH}$ as parameters.

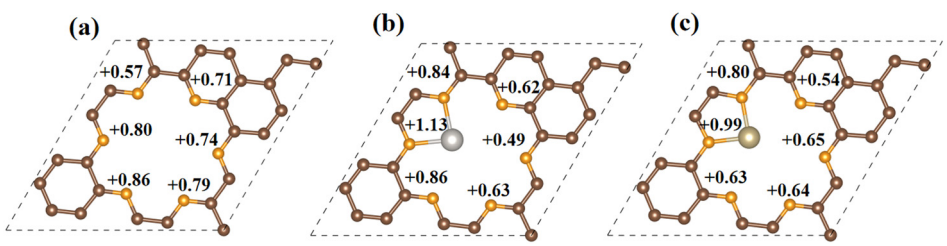

Fig. 10 Bader charge at each nitrogen atom calculated on (a) $C_{13}N_3$, (b) Pt-$C_{13}N_3$, and (c) Os-$C_{13}N_3$, respectively. The positive and negative values correspond to the charge gain and loss relative to the neutral atom, respectively. The unit is e^-, the electron charge.

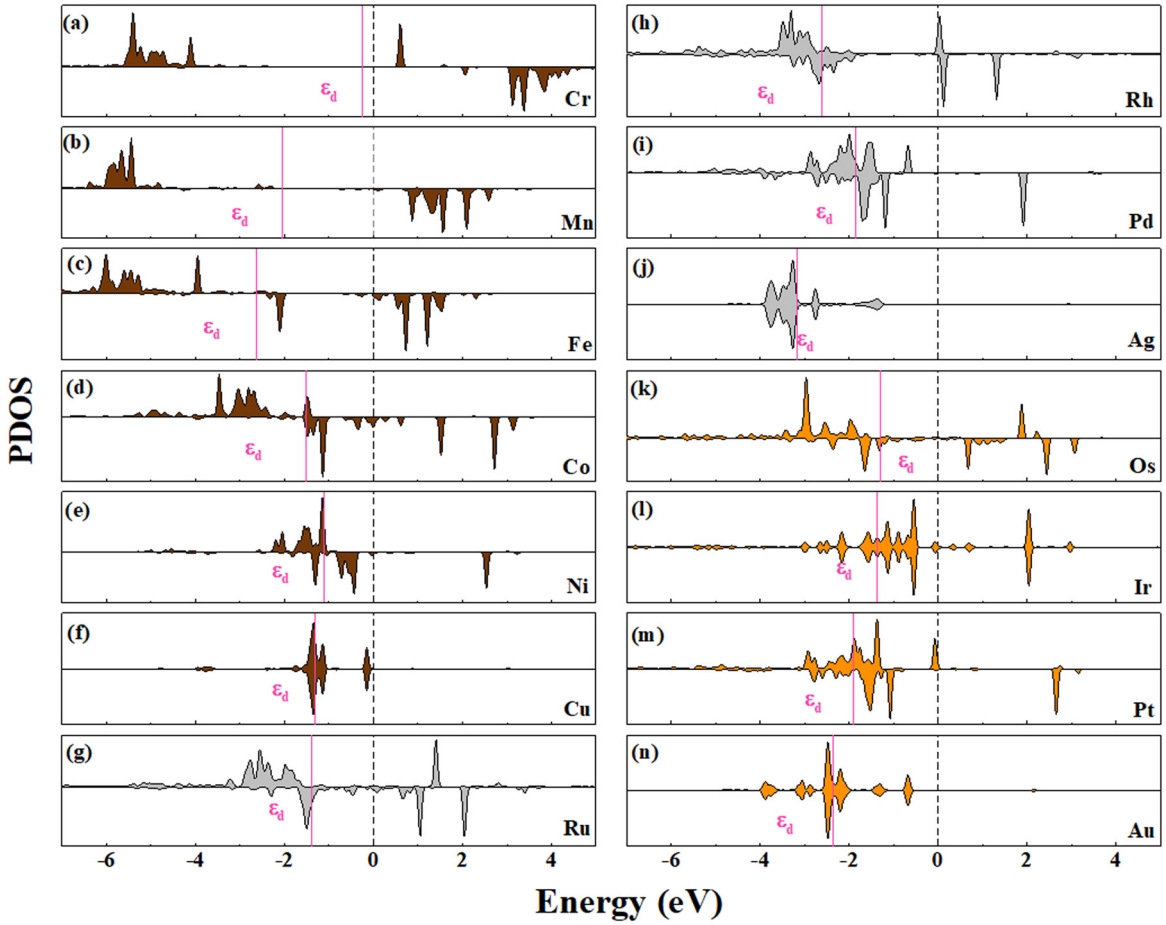

Fig. 11 Partial density of states (PDOS) of d orbitals for TM-$C_{13}N_3$. The d-band centers (ε_d) are also labeled for (a–f) 3d TM, from Cr to Cu; (g–j) 4d TM, from Ru to Ag; and (k–n) 5d TM, from Ag to Au. The Fermi level (E_F) is set to 0 eV.

the center of the d-band are shown in Table S4.† According to previous studies, it has been shown that as the number of d electrons increases, the center of the d-band gradually moves to the more negative position, which leads to weaker intermediate adsorption.[53–56] For example, the d-band centers of 5d transition metal atoms show the following trend: Os (−1.30) >Ir (−1.37) >Pt (−1.85) >Au (−2.38). For 3d and 4d transition metal atoms, different shifts of their d-band centers imply different adsorption strengths for the intermediates. Fundamentally, this is because when adsorption occurs, the d orbitals of the transition metal atoms interact with the electronic states of the intermediates, leading to orbital hybridization and the formation of bonding and antibonding states. The lower d-band center leads to a high occupation of the antibonding state, which reduces the adsorption energy. Obviously, the d-band center value of Pt-$C_{13}N_3$ is lower than that of Os-$C_{13}N_3$. This indicates that Pt-$C_{13}N_3$ has a more suitable adsorption strength for the intermediates compared to Os-$C_{13}N_3$.

We further calculated the bonding and antibonding states of the OH intermediates by the COHP method, which was used to analyze the structural bonding information,[57,58] where positive and negative values of -COHP indicate bonding and antibonding states, respectively. As shown in Fig. 12(a)–(c) and as shown in ESI† Fig. S3, TM-$C_{13}N_3$ is occupied by various degrees of antibonding states near the Fermi level. To obtain more quantitative information, the integrated value of -COHP below the Fermi level (-ICOHP) of the *OH intermediate was calculated as shown in Fig. 12(d) for all TMs studied here. The larger the -ICOHP value is, the stronger is the interaction strength between the TM and O atom of the *OH molecule.[59,60] The results show that the -ICOHP value on Os-$C_{13}N_3$ is larger than that on Pt-$C_{13}N_3$ (too strong interaction), while the value on Au-$C_{13}N_3$ is smaller (too weak interaction). The interaction between Pt-$C_{13}N_3$ and *OH is moderate. Therefore, charge transfer changes the electronic structure of TM-$C_{13}N_3$ SACs, which affects the adsorption strength of TM-$C_{13}N_3$ SACs on the reaction intermediates, leading to changes in catalytic activity.

E. Suppression of the HER and surface stability of Pt-$C_{13}N_3$

We discuss the catalytic activity of the HER and OER of Pt-$C_{13}N_3$ *via* the calculated adsorption energies. Hydrogen adsorption energy is a good descriptor for the HER, which has been widely used to describe the HER catalytic activity.[61]

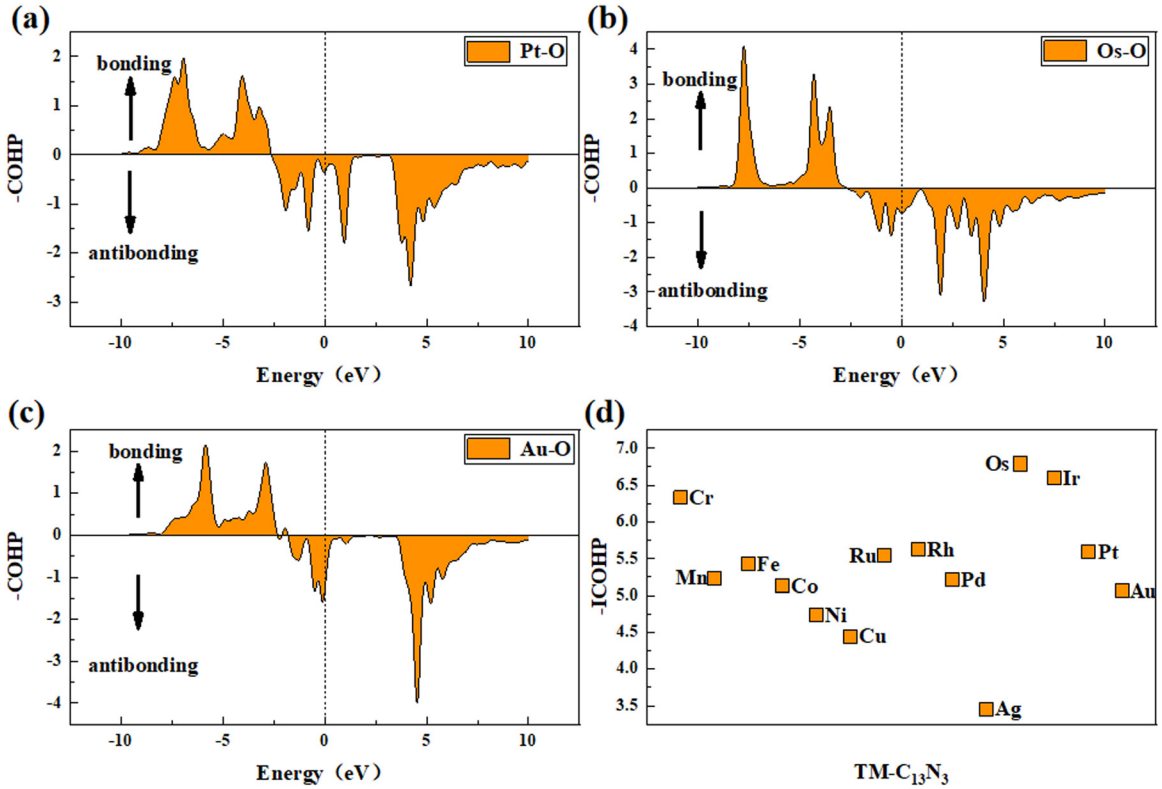

Fig. 12 -COHP of (a) Pt-$C_{13}N_3$, (b) Os-$C_{13}N_3$ and (c) Au-$C_{13}N_3$ with the reaction intermediate *OH, where the Fermi level is set to zero. (d) -ICOHP value of TM-$C_{13}N_3$ with the reaction intermediate *OH.

The Gibbs free energy of adsorbed hydrogen atoms was calculated as follows:

$$\Delta G_{*H} = \Delta E_{*H} + \Delta E_{ZPE} - T\Delta S \quad (24)$$

where ΔE_{*H} is the adsorption energy of H and ΔE_{ZPE} is the zero point energy difference between the adsorbed and gas phases. $\Delta S \approx -1/2S_{H_2}$, where S_{H_2} is the entropy of H_2. For the adsorption of hydrogen atoms on the surface, the Gibbs free energy can be written as $\Delta G_{*H} = \Delta E_{*H} + 0.24$ eV and for oxygen adsorption, the free energy is written as $\Delta G_{*O} = \Delta E_{*O} + 0.33$ eV, where E corresponds to the adsorption energy of adatom. As shown in Fig. 13, the Gibbs free energies of Pt-$C_{13}N_3$ are −1.57 eV and 0.14 eV for the HER and OER, respectively. A big negative ΔG shows a strong hydrogen binding to the catalytic surface and hence difficulty in generation and release, while a large positive ΔG represents the weak binding between the hydrogen atoms and catalytic surface.[62] Therefore, the ΔG for optimal HER and OER activity should be close to zero. Notably, the release of hydrogen inhibits the HER activity on Pt-$C_{13}N_3$, and it shows that Pt-$C_{13}N_3$ is a suitable material for the OER.

The surface stability of TM-$C_{13}N_3$ further depends on whether the doped metal (Pt) is covered by adsorbed species in aqueous solution under operating conditions. Therefore, we constructed surface Pourbaix plots of the doped metal as a function of pH and standard hydrogen electrode (U_{SHE}). As shown in Fig. 14, without applying a bias potential, *i.e.*, in a strongly acidic environment, the Pt atoms are covered by *OH groups, and as the pH increases, the *OH groups shift toward the *O groups.

However, as the electrode potential increases, the tendency of *O/*OH removal from the Pt surface increases, thus successively exposing the active center. In particular, the

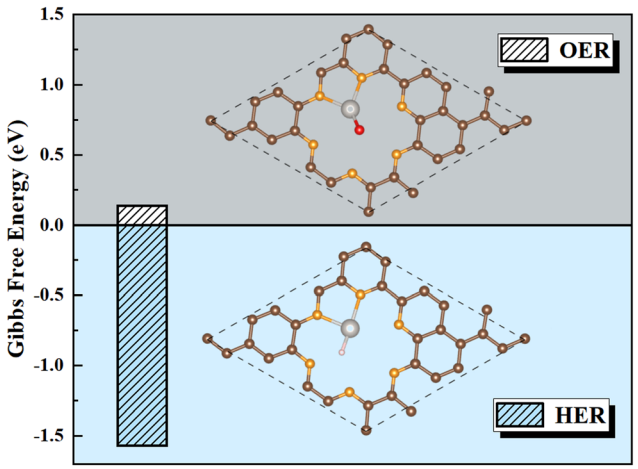

Fig. 13 Hydrogen adsorption free energy (ΔG_{*H}) *versus* O adsorption free energy (ΔG_{*O}). The inset shows a map of *H and *O adsorption sites on Pt-$C_{13}N_3$.

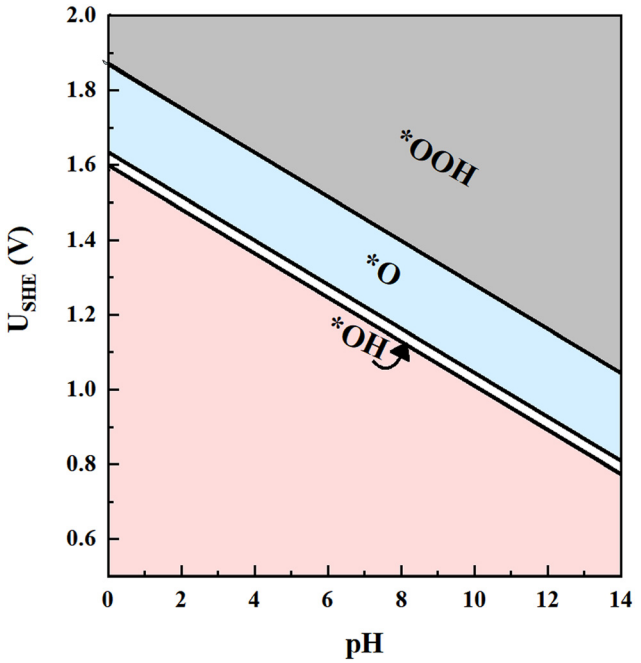

Fig. 14 Surface Pourbaix diagram of Pt atoms on $C_{13}N_3$, including alkaline and acidic dissolution.

minimum potential required for the removal of *O/*OH is 1.60 V for Pt atoms at pH = 0. This value is more positive than the limiting potential of 1.50 V for Pt-$C_{13}N_3$, demonstrating that Pt-$C_{13}N_3$ has an excellent stability against surface oxidation under operating conditions.

IV. Conclusion

In summary, we investigated the feasibility of a series of TMs (TM = Cr, Mn, Fe, Co, Ni, Cu, Ru, Rh, Pd, Ag, Os, Ir, Pt, and Au) embedded in $C_{13}N_3$ monolayers as highly efficient bifunctional OER and ORR catalysts. We first assessed the thermodynamic stability of the proposed TM-$C_{13}N_3$ nanosheets, finding that all of them have favorable energetics towards anchoring the TM atom. Molecular dynamics calculations show this stability to hold up to 1000 K. By calculating the transition states, it is demonstrated that the Pt atom does not easily diffuse into neighboring sites with a diffusion energy barrier as high as 2.95 eV. Their performance as electrocatalysts for the OER and ORR was evaluated by calculating their overpotentials, which were compared to the standard materials currently employed as unifunctional catalysts (Pt for the ORR and RuO_2 for the OER). Pt-$C_{13}N_3$ was found to be a promising bifunctional catalyst, having the low OER and ORR overpotentials of 0.27 V and 0.39 V, which are lower than the traditional unifunctional catalyst for each reaction individually. In addition to showing a lower overpotential, its bifunctional properties would allow its usage as either the anode in an electrolyzer cell or the cathode of a fuel cell, which could be unified in single apparatus. Since the material proposed here has a large percentage of earth-abundant elements (carbon and nitrogen), it is also possible that it could benefit from being cheaper than the conventional ones made of only noble metals.

Volcano plots and contour maps were created based on the scalar relationships between oxygenated intermediates (*OH, *O, and *OOH). In addition, Bader charge analysis, d-band center, and ICOHP methods were used to reveal the origin of OER and ORR activity. We have investigated and characterized the OER and ORR properties of TM-$C_{13}N_3$, which provide theoretical guidance for future clean energy technology conversion and the development of new efficient electrocatalysts.

Data availability

All relevant data are within the manuscript and its ESI† files.

Conflicts of interest

There are no conflicts of interest to declare.

Acknowledgements

We acknowledge support from Shandong Province's Double Hundred Experts project WSP2023008. Xianfang Yue would like to thank Jining University for its support (2022HHKJ03). BRLG is grateful to Conselho Nacional de Desenvolvimento Científico e Tecnológico (CNPq) grant 311508-2021-9 and Fundação de Amparo à Pesquisa do estado de Minas Gerais (FAPEMIG) grants APQ-00597-22, APQ-03705-23, and RED-00045-23.

References

1 S. Chu and A. Majumdar, Opportunities and challenges for a sustainable energy future, *Nature*, 2012, **488**, 294.
2 Z. Yang, J. Zhang, M. C. W. Kintner-Meyer, X. Lu, D. Choi, J. P. Lemmon and J. Liu, Electrochemical Energy Storage for Green Grid, *Chem. Rev.*, 2011, **111**, 3577.
3 A. Züttel, A. Remhof, A. Borgschulte and O. Friedrichs, Hydrogen: The future energy carrier, *Philos. Trans. R. Soc., A*, 2010, **368**, 3329.
4 T. N. Veziroğlu and S. Şahi·n, 21st Century's energy: Hydrogen energy system, *Energy Convers. Manage.*, 2008, **49**, 1820.
5 A. Midilli and I. Dincer, Hydrogen as a renewable and sustainable solution in reducing global fossil fuel consumption, *Int. J. Hydrogen Energy*, 2008, **33**, 4209.
6 N. Muradov, Low to near-zero CO_2 production of hydrogen from fossil fuels: Status and perspectives, *Int. J. Hydrogen Energy*, 2017, **42**, 14058.
7 S. Wang, A. Lu and C.-J. Zhong, Hydrogen production from water electrolysis: Role of catalysts, *Nano Convergence*, 2021, **8**, 4.
8 G. L. Soloveichik, Regenerative Fuel Cells for Energy Storage, *Proc. IEEE*, 2014, **102**, 964.

9 L. Yaqoob, T. Noor and N. Iqbal, An overview of metalair batteries, current progress, and future perspectives, *J. Energy Storage*, 2022, **56**, 106075.
10 S. R. Ede and Z. Luo, Tuning the intrinsic catalytic activities of oxygen-evolution catalysts by doping: A comprehensive review, *J. Mater. Chem. A*, 2021, **9**, 20131.
11 Y. Li, Y. Feng, D. Zheng, X. Zhao, Y. Zhou, X. Fu and X. Chen, High-performance screening of carbon-nitride single-atom catalysts for oxygen electrode reaction in rechargeable metal–air batteries, *Chem. Eng. J.*, 2023, **476**, 146753.
12 X. Zhang, A. Chen, Z. Zhang, M. Jiao and Z. Zhou, Transition metal anchored C2N monolayers as efficient bifunctional electrocatalysts for hydrogen and oxygen evolution reactions, *J. Mater. Chem. A*, 2018, **6**, 11446.
13 T. He, S. K. Matta, G. Will and A. Du, Transition-Metal Single Atoms Anchored on Graphdiyne as High-Efficiency Electrocatalysts for Water Splitting and Oxygen Reduction, *Small Methods*, 2019, **3**, 1800419.
14 X. Liu, Y. Zhang, W. Wang, Y. Chen, W. Xiao, T. Liu, Z. Zhong, Z. Luo, Z. Ding and Z. Zhang, Transition Metal and N Doping on AlP Monolayers for Bifunctional Oxygen Electrocatalysts: Density Functional Theory Study Assisted by Machine Learning Description, *ACS Appl. Mater. Interfaces*, 2022, **14**, 1249.
15 K. Elumeeva, J. Masa, D. Medina, E. Ventosa, S. Seisel, Y. U. Kayran, A. Genç, T. Bobrowski, P. Weide, J. Arbiol, M. Muhler and W. Schuhmann, Cobalt boride modified with N-doped carbon nanotubes as a highperformance bifunctional oxygen electrocatalyst, *J. Mater. Chem. A*, 2017, **5**, 21122.
16 B.-Q. Li, C.-X. Zhao, S. Chen, J.-N. Liu, X. Chen, L. Song and Q. Zhang, Framework-Porphyrin-Derived Single-Atom Bifunctional Oxygen Electrocatalysts and their Applications in Zn–Air Batteries, *Adv. Mater.*, 2019, **31**, 1900592.
17 X. Sun, S. Sun, S. Gu, Z. Liang, J. Zhang, Y. Yang, Z. Deng, P. Wei, J. Peng, Y. Xu, C. Fang, Q. Li, J. Han, Z. Jiang and Y. Huang, High-performance single atom bifunctional oxygen catalysts derived from ZIF-67 superstructures, *Nano Energy*, 2019, **61**, 245.
18 K. Zeng, X. Zheng, C. Li, J. Yan, J.-H. Tian, C. Jin, P. Strasser and R. Yang, Recent Advances in Non-Noble Bifunctional Oxygen Electrocatalysts toward Large-Scale Production, *Adv. Funct. Mater.*, 2020, **30**, 2000503.
19 X. Wan, H. Niu, Y. Yin, X. Wang, C. Shao, Z. Zhang and Y. Guo, Enhanced electrochemical oxygen evolution reaction activity on natural single-atom catalysts transition metal phthalocyanines: The substrate effect, *Catal. Sci. Technol.*, 2020, **10**, 8339.
20 B. Qiao, A. Wang, X. Yang, L. F. Allard, Z. Jiang, Y. Cui, J. Liu, J. Li and T. Zhang, Single-atom catalysis of CO oxidation using Pt1/FeOx, *Nat. Chem.*, 2011, **3**, 634.
21 X. Cui, W. Li, P. Ryabchuk, K. Junge and M. Beller, Bridging homogeneous and heterogeneous catalysis by heterogeneous single-metal-site catalysts, *Nat. Catal.*, 2018, **1**, 385.
22 D. Liu, Q. He, S. Ding and L. Song, Structural Regulation and Support Coupling Effect of Single-Atom Catalysts for Heterogeneous Catalysis, *Adv. Energy Mater.*, 2020, **10**, 2001482.
23 X.-F. Yang, A. Wang, B. Qiao, J. Li, J. Liu and T. Zhang, Single-Atom Catalysts: A New Frontier in Heterogeneous Catalysis, *Acc. Chem. Res.*, 2013, **46**, 1740.
24 H. Niu, X. Wan, X. Wang, C. Shao, J. Robertson, Z. Zhang and Y. Guo, Single-Atom Rhodium on Defective g-C_3N_4: A Promising Bifunctional Oxygen Electrocatalyst, *ACS Sustainable Chem. Eng.*, 2021, **9**, 3590.
25 Y. Zhou, G. Gao, J. Kang, W. Chu and L.-W. Wang, Computational screening of transition-metal single atom doped C_9N_4 monolayers as efficient electrocatalysts for water splitting, *Nanoscale*, 2019, **11**, 18169.
26 R. Tan, Z. Li, P. Zhou, Z. Zou, W. Li and L. Sun, Dirac Semimetals in Homogeneous Holey Carbon Nitride Monolayers, *J. Phys. Chem. C*, 2021, **125**, 6082.
27 Q. Li, L. Zhang, J. Liu, J. Zhou, Y. Jiao, X. Xiao, C. Zhao, Y. Zhou, S. Ye, B. Jiang and J. Liu, Porous Carbon Nitride Thin Strip: Precise Carbon Doping Regulating Delocalized π-Electron Induces Elevated Photocatalytic Hydrogen Evolution, *Small*, 2021, **17**, 2006622.
28 G. Kresse and J. Furthmüller, Efficiency of ab-initio total energy calculations for metals and semiconductors using a plane-wave basis set, *Comput. Mater. Sci.*, 1996, **6**, 15.
29 G. Kresse and J. Furthmüller, Efficient iterative schemes for ab initio total-energy calculations using a plane-wave basis set, *Phys. Rev. B: Condens. Matter Mater. Phys.*, 1996, **54**, 11169.
30 P. E. Blöchl, Projector augmented-wave method, *Phys. Rev. B: Condens. Matter Mater. Phys.*, 1994, **50**, 17953.
31 J. P. Perdew, K. Burke and M. Ernzerhof, Generalized Gradient Approximation Made Simple, *Phys. Rev. Lett.*, 1996, **77**, 3865.
32 M. Cococcioni and S. De Gironcoli, Linear response approach to the calculation of the effective interaction parameters in the LDA + U method, *Phys. Rev. B: Condens. Matter Mater. Phys.*, 2005, **71**, 035105.
33 S. Maintz, V. L. Deringer, A. L. Tchougréeff and R. Dronskowski, LOBSTER: A tool to extract chemical bonding from plane-wave based DFT, *J. Comput. Chem.*, 2016, **37**, 1030.
34 G. Kresse and J. Hafner, Ab Initio molecular dynamics for liquid metals, *Phys. Rev. B: Condens. Matter Mater. Phys.*, 1993, **47**, 558.
35 C. Su, H. Jiang and J. Feng, Two-dimensional carbon allotrope with strong electronic anisotropy, *Phys. Rev. B: Condens. Matter Mater. Phys.*, 2013, **87**, 075453.
36 W. Tang, E. Sanville and G. Henkelman, A grid-based Bader analysis algorithm without lattice bias, *J. Phys.: Condens. Matter*, 2009, **21**, 084204.
37 H. W. Kim, V. J. Bukas, H. Park, S. Park, K. M. Diederichsen, J. Lim, Y. H. Cho, J. Kim, W. Kim, T. H. Han, J. Voss, A. C. Luntz and B. D. McCloskey, Mechanisms of Two-Electron and Four-Electron Electrochemical Oxygen Reduction Reactions at Nitrogen-Doped Reduced Graphene Oxide, *ACS Catal.*, 2020, **10**, 852.

38 L. Yu, X. Pan, X. Cao, P. Hu and X. Bao, Oxygen reduction reaction mechanism on nitrogen-doped graphene: A density functional theory study, *J. Catal.*, 2011, **282**, 183.
39 J. K. Nørskov, J. Rossmeisl, A. Logadottir, L. Lindqvist, J. R. Kitchin, T. Bligaard and H. Jónsson, Origin of the Overpotential for Oxygen Reduction at a Fuel-Cell Cathode, *J. Phys. Chem. B*, 2004, **108**, 17886.
40 K. S. Exner, Chlorine Evolution Reaction on RuO_2 (110): Ab initio Atomistic Thermodynamics Study – Pourbaix Diagrams, *Electrochim. Acta*, 2014, **120**, 460.
41 T. Lim, G. Y. Jung, J. H. Kim, S. O. Park, J. Park, Y.-T. Kim, S. J. Kang, H. Y. Jeong, S. K. Kwak and S. H. Joo, Atomically dispersed $Pt–N_4$ sites as efficient and selective electrocatalysts for the chlorine evolution reaction, *Nat. Commun.*, 2020, **11**, 412.
42 X. Liu, Y. Zhang, W. Wang, Y. Chen, W. Xiao, T. Liu, Z. Zhong, Z. Luo, Z. Ding and Z. Zhang, Transition Metal and N Doping on AlP Monolayers for Bifunctional Oxygen Electrocatalysts: Density Functional Theory Study Assisted by Machine Learning Description, *ACS Appl. Mater. Interfaces*, 2022, **14**, 1249.
43 A. Wang, H. Niu, X. Wang, X. Wan, L. Xie, Z. Zhang, J. Wang and Y. Guo, Two-dimensional metal–organic frameworks as efficient electrocatalysts for bifunctional oxygen evolution/reduction reactions, *J. Mater. Chem. A*, 2022, **10**, 13005.
44 H. Niu, X. Wan, X. Wang, C. Shao, J. Robertson, Z. Zhang and Y. Guo, Single-Atom Rhodium on Defective $g\text{-}C_3N_4$: A Promising Bifunctional Oxygen Electrocatalyst, *ACS Sustainable Chem. Eng.*, 2021, **9**, 3590.
45 C. Guan, R. Ouyang, H. Zhu and Y. Xie, Theoretical inspection of $TM\text{-}P_4C$ single-atom electrocatalysts: High performance for oxygen reduction and evolution reactions, *Electrochim. Acta*, 2022, **427**, 140853.
46 D. Sheppard, R. Terrell and G. Henkelman, Optimization methods for finding minimum energy paths, *J. Chem. Phys.*, 2008, **128**, 134106.
47 J. Rossmeisl, A. Logadottir and J. Nørskov, Electrolysis of water on (oxidized) metal surfaces, *Chem. Phys.*, 2005, **319**, 178.
48 I. C. Man, H.-Y. Su, F. Calle-Vallejo, H. A. Hansen, J. I. Martínez, N. G. Inoglu, J. Kitchin, T. F. Jaramillo, J. K. Nørskov and J. Rossmeisl, Universality in Oxygen Evolution Electrocatalysis on Oxide Surfaces, *ChemCatChem*, 2011, **3**, 1159.
49 K. Li, Y. Li, Y. Wang, F. He, M. Jiao, H. Tang and Z. Wu, The oxygen reduction reaction on Pt(111) and Pt(100) surfaces substituted by subsurface Cu: A theoretical perspective, *J. Mater. Chem. A*, 2015, **3**, 11444.
50 A. J. Medford, A. Vojvodic, J. S. Hummelshøj, J. Voss, F. Abild-Pedersen, F. Studt, T. Bligaard, A. Nilsson and J. K. Nørskov, From the Sabatier principle to a predictive theory of transition-metal heterogeneous catalysis, *J. Catal.*, 2015, **328**, 36.
51 Q. Deng, J. Zhao, T. Wu, G. Chen, H. A. Hansen and T. Vegge, 2D transition metal–TCNQ sheets as bifunctional single-atom catalysts for oxygen reduction and evolution reaction (ORR/OER), *J. Catal.*, 2019, **370**, 378.
52 X. Lv, W. Wei, H. Wang, B. Huang and Y. Dai, Holey graphitic carbon nitride (g-CN) supported bifunctional single atom electrocatalysts for highly efficient overall water splitting, *Appl. Catal., B*, 2020, **264**, 118521.
53 C. Ling, L. Shi, Y. Ouyang, X. C. Zeng and J. Wang, Nanosheet Supported Single-Metal Atom Bifunctional Catalyst for Overall Water Splitting, *Nano Lett.*, 2017, **17**, 5133.
54 X. Mao, C. Ling, C. Tang, C. Yan, Z. Zhu and A. Du, Predicting a new class of metal-organic frameworks as efficient catalyst for bi-functional oxygen evolution/reduction reactions, *J. Catal.*, 2018, **367**, 206.
55 Z. Fu, C. Ling and J. Wang, A $Ti_3C_2O_2$ supported single atom, trifunctional catalyst for electrochemical reactions, *J. Mater. Chem. A*, 2020, **8**, 7801.
56 I. Yamada, A. Takamatsu, K. Asai, T. Shirakawa, H. Ohzuku, A. Seno, T. Uchimura, H. Fujii, S. Kawaguchi, K. Wada, H. Ikeno and S. Yagi, Systematic Study of Descriptors for Oxygen Evolution Reaction Catalysis in Perovskite Oxides, *J. Phys. Chem. C*, 2018, **122**, 27885.
57 R. Dronskowski and P. E. Bloechl, Crystal orbital Hamilton populations (COHP): Energy-resolved visualization of chemical bonding in solids based on density-functional calculations, *J. Phys. Chem.*, 1993, **97**, 8617.
58 F. Li, H. Ai, D. Liu, K. H. Lo and H. Pan, An enhanced oxygen evolution reaction on 2D CoOOH via strain engineering: An insightful view from spin state transition, *J. Mater. Chem. A*, 2021, **9**, 17749.
59 R. Hu, Y. Li, Q. Zeng and J. Shang, Role of active sites in N-coordinated Fe-Co dual-metal doped graphene for oxygen reduction and evolution reactions: A theoretical insight, *Appl. Surf. Sci.*, 2020, **525**, 146588.
60 X. Liu, Y. Zhang, T. Liu, W. Wang, Z. Luo, Z. Zhang and W. Xiao, Rational design synergistic metal-free dualatom electrocatalyst for N2 to NH3 reaction on g-CN: A first principle study, *Appl. Surf. Sci.*, 2022, **605**, 154831.
61 X. Zou and Y. Zhang, Noble metal-free hydrogen evolution catalysts for water splitting, *Chem. Soc. Rev.*, 2015, **44**, 5148.
62 P. E. Blöchl, First-principles calculations of defects in oxygen-deficient silica exposed to hydrogen, *Phys. Rev. B: Condens. Matter Mater. Phys.*, 2000, **62**, 6158.